# Numerical Simulation of an Inclined Rigid Filament under Biomagnetic Fluid Flow

Dinesh Kumar RAVADA, Ranjith MANIYERI*

*Biophysics Laboratory, Department of Mechanical Engineering, National Institute of Technology Karnataka (NITK), Surathkal, Mangalore, Karnataka, India*
*\*Corresponding Author e-mail: mranji1@nitk.edu.in*

The present study investigates the impact of magnetic field on the interaction of stationary, rigid filament-like structures in biomagnetic fluid flow, which has broad applications in mixing, transport, targeted drug delivery, and the development of magnetic devices. This work focuses on modeling a stationary, rigid, inclined filament fixed at the bottom of a channel within biomagnetic flow using the immersed boundary method. The inclined filament is positioned at various angles ($\theta = 45°$, $90°$, and $135°$) in biomagnetic flow. Numerical simulations reveal that the fluid-filament interaction exhibits increased recirculation zones downstream when influenced by a magnetic field. Interestingly, when the filament is placed at $\theta = 45°$, there is a reduction in vortex formation upstream. The study also examines the effect of parameters such as the Reynolds number (Re) and the magnetic number (Mn) on the size of vortex formation. It is evident that as the Re and Mn increase the size of recirculation zones and secondary vortex formation also increases.

**Keywords:** biomagnetic fluid, rigid inclined filament, immersed boundary method, magnetic number.

## 1. Introduction

Numerous studies have examined the effects of induced electric and magnetic fields on biological activities in the human body. It is well-established that biological fluids, when exposed to a magnetic field, produce considerable effects depending on their magnetic behavior and the field's strength. Human blood is a mixture of red blood cells (RBCs), white blood cells (WBCs), and platelets suspended in a saline solution known as plasma [1]. RBCs contain hemoglobin, an iron-rich protein responsible for transporting oxygen and carbon dioxide between the lungs and capillaries. According to Pauling and Coryell [2], blood acts as a diamagnetic fluid when oxygenated and as a paramagnetic fluid when deoxygenated. Due to this magnetic characteristic, blood is classified as a bio-

magnetic fluid. Haik *et al.* [1] were the first to introduce the possibility of using biomagnetic fluid dynamics for the study of blood flow in a static magnetic field. Additionally, they explained its application in the biomedical field. Potential applications of biomagnetic fluid flow include site-specific drug delivery, blood stasis prevention, magnetic seals, retinal tear repair and magnetic thrombi treatment.

Many numerical and experimental studies have explored biomagnetic fluid flow due to its potential applications. Loukopoulos and Tzirtzilakis [3] explored the numerical simulation of steady fluid flow in a channel placed in a spatially varying magnetic field. Tzirtzilakis [4] extended this work to study the flow of biomagnetic fluid in a stenosed channel using the finite difference method, where the mathematical formulation is based on the principles of magnetohydrodynamics (MHD) and ferrohydrodynamics (FHD). The work explained the effects of temperature, the skin friction coefficient, and the rate of heat transfer along the fluid flow in the presence of a magnetic field. Further, Habibi *et al.* [5] investigated the effects of a non-uniform magnetic field on blood flow. It was discovered that at low Reynolds numbers (Re), blood pressure decreases as it moves away from the magnetic source and increases in proximity to it. Additionally, they considered the electrical and magnetic properties of blood and the effects of wall shear stress on biomagnetic fluid. Subsequently, Kenjeres [6] developed a mathematical model to describe blood flow in arteries exposed to a strong magnetic field. Their study provided information about the variations in local pressure and the development of secondary flow patterns near regions influenced by the of magnetic field.

Mousavi *et al.* [7] proposed a 3D numerical model to investigate the influence of Lorentz force and magnetic force generated due to magnetization of a magnetic field. They found that secondary flow formation increases non-axial shear stress near the walls. In our previous work, we used the finite volume method to simulate the flow of biomagnetic fluid in a non-uniform magnetic field under shear flow conditions [8]. The present work extends our previous work [8] by examining the influence of a stationary rigid filament placed in the biomagnetic fluid flow. The numerical model for this fluid-structure interaction problem is developed using the immersed boundary method (IBM). IBM is the most popular method used for modeling the interaction between immersed structures and the surrounding fluid without generating complex mesh.

Peskin [9] developed an IBM to examine blood flow in heart valves. Later, Lai and Peskin [10] developed a precise second-order IBM for flow over a cylinder to analyze the effects of numerical viscosity. Maniyeri and Kang [11,12] used IBM to investigate the rotation of an elastic rod and to explore the bundling and tumbling motion of bacterial flagella in a viscous fluid. The IBM developed by Peskin was employed by Kanchan and Maniyeri [13] to investigate the

recovery dynamics of a flexible filament. Additionally, Basil *et al.* [14] studied the effect of rigid filament in oscillatory flow. Kanchan and Maniyeri [15] explored the asymmetrical behavior of a flexible filament in shear flow. From the literature review, it is evident that the interaction of immersed structures with biomagnetic fluid flow has not been widely reported. The presence of a rigid filament with different orientations under an imposed biomagnetic flow could have potential applications in controling flow dynamics for biomedical applications. With this perspective, the key objective of this study is to develop a 2D immersed boundary finite volume numerical model to simulate biomagnetic fluid flow in a 2D channel with rigid stationary filament positioned at three different angles ($\theta = 45°$, $90°$, and $135°$). The influence of the magnetic field on fluid flow is examined by varying Re and magnetic number (Mn) for different filament orientations.

## 2. Mathematical formulation

We consider a 2D unsteady biomagnetic flow, and the relevant governing equations in dimensionless form presented below [7].

Continuity equation:

$$\frac{\partial u}{\partial x} + \frac{\partial v}{\partial y} = 0, \tag{1}$$

where $u$ and $v$ represent the velocity components in the $x$- and $y$-directions, respectively.

Momentum equation in $x$-direction:

$$\frac{\partial u}{\partial t} + u\frac{\partial u}{\partial x} + v\frac{\partial u}{\partial y} = -\frac{\partial p}{\partial x} + \frac{1}{\text{Re}}\left(\frac{\partial^2 u}{\partial x^2} + \frac{\partial^2 u}{\partial y^2}\right) + \text{MnH}\frac{\partial \text{H}}{\partial x} + f_x. \tag{2}$$

Momentum equation in $y$-direction:

$$\frac{\partial v}{\partial t} + u\frac{\partial v}{\partial x} + v\frac{\partial v}{\partial y} = -\frac{\partial p}{\partial y} + \frac{1}{\text{Re}}\left(\frac{\partial^2 v}{\partial}x^2 + \frac{\partial^2 v}{\partial y^2}\right) + \text{MnH}\frac{\partial \text{H}}{\partial y} + f_y, \tag{3}$$

where $\text{Mn} = \frac{\mu_0^2 H_0^2 \varkappa}{\rho U^2 \mu_0}$, $\text{Re} = \frac{Uh}{\nu}$, H represents magnetic intensity and $\varkappa$ denotes magnetic susceptibility [1], $\rho$ is the fluid density, $\mu_0$ is the magnetic permeability, and $f_x$ and $f_y$ are the components of the Eulerian force $\mathbf{f}(\mathbf{x}, t)$ in the $x$- and $y$-directions, respectively. These components are calculated using the Lagrangian force $\mathbf{F}(s, t)$, where $s$ denotes the Lagrangian material point,

$$\mathbf{f}(\mathbf{x}, t) = \int \mathbf{F}(s, t)\delta(\mathbf{x} - \mathbf{X}(s, t))ds, \tag{4}$$

where $\mathbf{x} = (x, y)$ represents the Eulerian coordinates, and $\mathbf{X}(s, t)$ represents the Lagrangian coordinates of the immersed body. The non-dimensional form of magnetic intensity in the $x$- and $y$-directions is taken from [4]. Since the filament is rigid and stationary, the Lagrangian force is calculated as the tether force, given by:

$$\mathbf{F}(s, t) = K \left( \mathbf{X}_e(s, t) - \mathbf{X}(s, t) \right), \tag{5}$$

where $K$ is the stiffness constant, and $\mathbf{X}_e(s, t)$, $\mathbf{X}(s, t)$ are the initial and updated position of the immersed boundary (IB) points. To keep the rigid filament in equilibrium and close to its initial position, the stiffness constant must be quite high ($K \gg 1$). $\delta$ represents regularized delta function which is given below as:

$$\delta(\mathbf{x}) = \frac{1}{\Delta x \Delta y} \Phi \left( \frac{(x - \mathbf{X}(s, t))}{\Delta x} \right) \Phi \left( \frac{(y - \mathbf{Y}(s, t))}{\Delta y} \right), \tag{6}$$

where

$$\Phi(r) = \begin{cases} \frac{1}{8} \left( 3 - 2 |r| + \sqrt{1 + 4 |r| - 4r^2} \right), & 0 \leq |r| \leq 1, \\ \frac{1}{8} \left( 5 - 2 |r| - \sqrt{-7 + 12 |r| - 4r^2} \right), & 1 \leq |r| \leq 2, \\ 0, & \text{otherwise,} \end{cases}$$

$$\mathbf{U}^{n+1}(s, t) = \int \mathbf{u}^{n+1}(\mathbf{x}, t) \delta(\mathbf{x} - \mathbf{X}^n(s, t)) d\mathbf{x}, \tag{7}$$

$$\mathbf{U}^{n+1}(s, t) = \frac{\mathbf{X}^{n+1}(s, t) - \mathbf{X}^n(s, t)}{\Delta t}. \tag{8}$$

In the above expression, the fluid velocity field obtained by solving Eqs. (1)–(3) is denoted by $\mathbf{u}^{n+1}(\mathbf{x}, t)$. The Lagrangian velocity variable is represented as $\mathbf{U}^{n+1}(s, t)$, and $\mathbf{X}^{n+1}(s, t)$ denotes new coordinates of the Lagrangian variable.

Accordingly, we chose a channel domain of $10 \times 1$, where no-slip boundary conditions are applied at the top and bottom walls. For the numerical simulation, a FORTRAN code is developed to solve the non-dimensional form of the governing differential equations (Eqs. (1)–(8)), which are discretized using the semi-implicit fractional step method based on the finite volume scheme on a staggered grid system. The discretized momentum equations coupled with the Eulerian force density function are solved using ICCG scheme [16].

## 3. Results and discussion

### 3.1. Model validation

Initially, using the model, a simple Poiseuille flow in a channel is simulated with an inlet velocity ($U = 1.0$), and Re = 10. The no-slip boundary condition is maintained at the top and bottom of the walls. The velocity profile at location $x = 5.0$, plotted against $y$-axis, is compared with the analytical results and is shown in Fig. 1a. Figure 1b shows the steady-state parabolic velocity vector plot at different channel sections. Figure 1c presents the steady-state streamline plot. All of these plots confirm the validity of the developed numerical model.
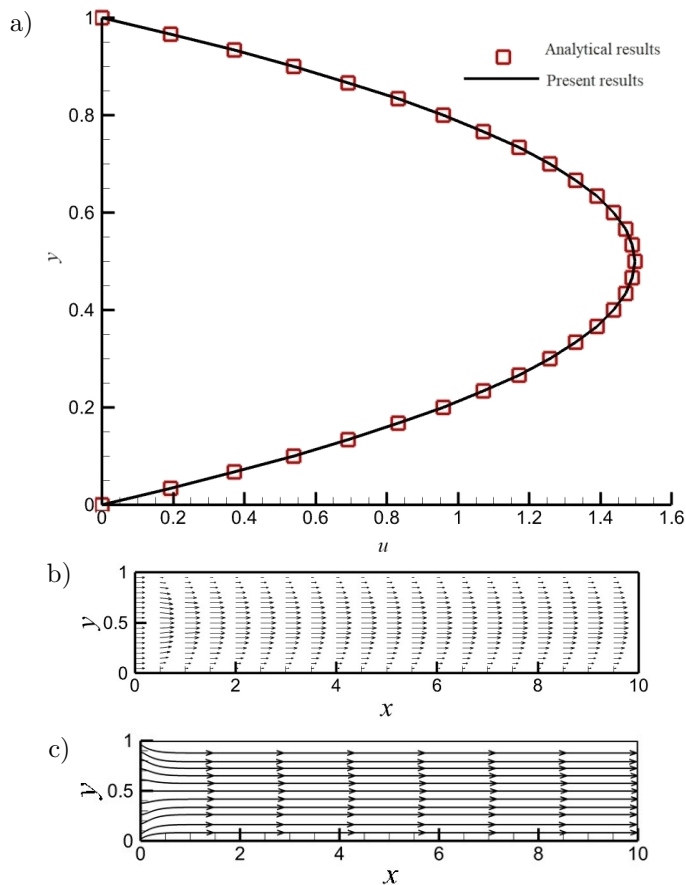
FIG. 1. a) Validation plot for centerline velocity, b) vector plot, c) streamline plot for Poiseuille flow.

To implement the IBM scheme in the channel flow, we introduced a virtual wall at the center of the channel, where the virtual wall is modelled as an IB. Figure 2 shows the vector and contour plots of the channel flow sepa-
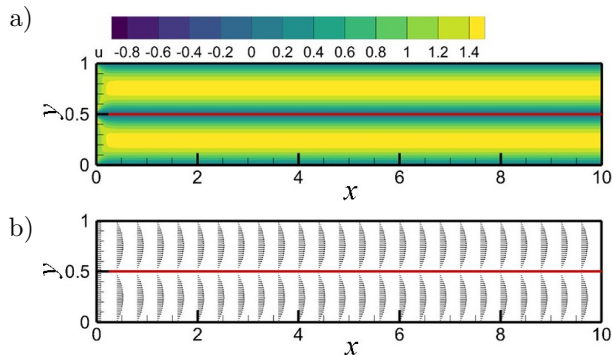
a)



b)

Fig. 2. a) Velocity contour, b) vector plot.

rated by a virtual wall. From the figure, it can be observed that the no-slip condition at the virtual wall is well enforced through the implementation of IBM. Also, a parabolic velocity profile is developed (Fig. 2b) above and below the middle virtual wall modelled using IBM. This shows that IBM can be easily implemented in the channel flow domain.

We have selected an additional benchmark problem involving flow over a stationary circular cylinder, which provides an excellent test case for evaluating the solver's ability to handle complex flow-structure interaction. In this case, we considered a rectangular domain of $14 \times 7$ with a circular cylinder of diameter 1.0 placed at $(3.5, 3.5)$. We imposed Neumann boundary conditions along the lateral walls of the channel, with a uniform velocity ($U = 1.0$) at the entrance.

A grid independence study was conducted to ensure the accuracy and reliability of the model. The simulation was carried out for Re = 40, revealing the formation of symmetric vortices downstream of the cylinder, leading to flow separation along its length, as shown in Fig. 3. We computed the wake length, as shown in Fig. 3. Table 1 shows the wake lengths for different grid sizes.
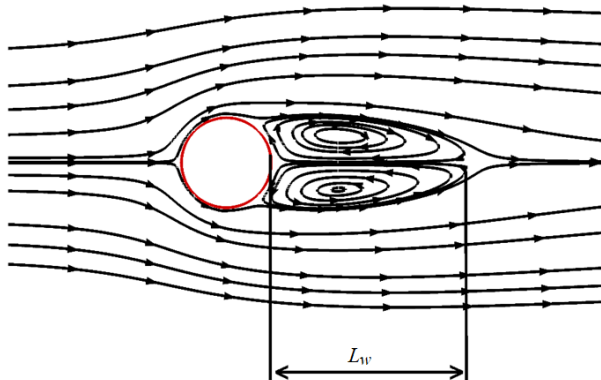


Fig. 3. Calculation of wake length.

TABLE 1. Comparison of recirculation sizes of different grid sizes for Re = 40.

| Grid | $281 \times 141$ | $561 \times 281$ | $701 \times 351$ |
|---|---|---|---|
| Recirculation length $(2L_w/D)$ | 4.52 | 4.46 | 4.44 |

The values of wake length are very similar for grid sizes $561 \times 281$ and $701 \times 351$. Based on the computational time, we have chosen $561 \times 281$ as the optimal grid configuration.

As part of the validation, we performed simulations for Reynolds numbers (Re = 10, 20, and 40) and calculated the wake length, as reported in Table 2. It is observed that the current simulation results are in good agreement with those of previous researchers. This further confirms the validity of the developed model.

TABLE 2. Validation for wake length.

| Re | Comparison of recirculation length | | |
|---|---|---|---|
| | Guo *et al.* [17] | Coutanceau and Bouard [18] | Present results |
| | Recirculation length $(2L_w/D)$ | Recirculation length $(2L_w/D)$ | Recirculation length $(2L_w/D)$ |
| 10 | 0.53 | 0.68 | 0.64 |
| 20 | 1.86 | 1.86 | 2.12 |
| 40 | 4.40 | 4.26 | 4.46 |

## 3.2. Grid independence study

A grid independence study was performed with the filament positioned at $135°$ (clockwise direction), as shown in Fig. 4.
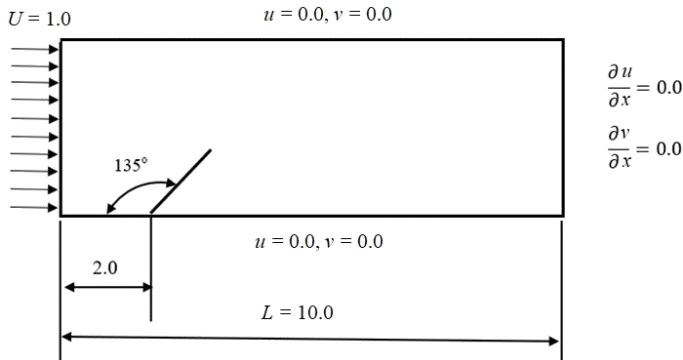


FIG. 4. Schematic of the inclined filament placed at an angle of $135°$ (clockwise direction).

We performed simulation on Eulerian grids of $601 \times 61$, $501 \times 51$, and $301 \times 31$ for different combinations of Reynolds numbers and magnetic numbers (Re = 10,

Mn $= 1000$ and Re $= 50$, Mn $= 500$). We plotted the $u$-velocity at a location nearest to the magnetic source $(2.5, 0.0)$ against the $y$-axis, as illustrated in Fig. 5. The figure indicates negligible variation in the velocity profile for the grids $601 \times 61$ and $501 \times 51$. Considering computational time constraints, we have selected the optimal grid as $501 \times 51$.
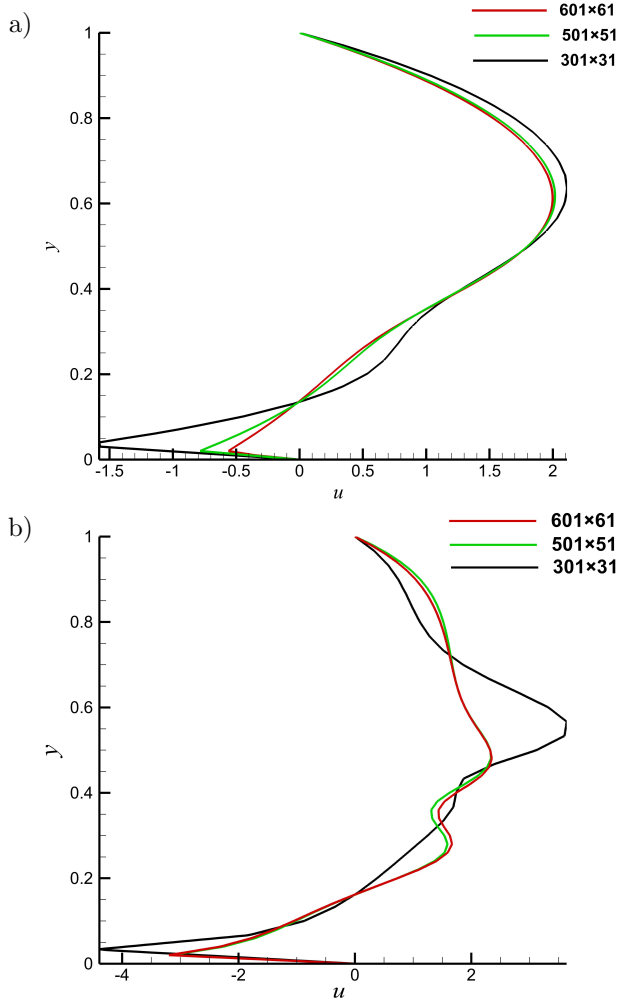


FIG. 5. Velocity profile at $(2.5, 0.0)$ for a) Re $= 10$ and Mn $= 1000$, b) Re $= 50$ and Mn $= 500$.

## 3.3. Inclined filament under biomagnetic flow

In this section, the simulation of an inclined filament under biomagnetic fluid flow is investigated using the developed numerical model. Figure 6 shows the distribution of magnetic field lines when a magnetic source is introduced
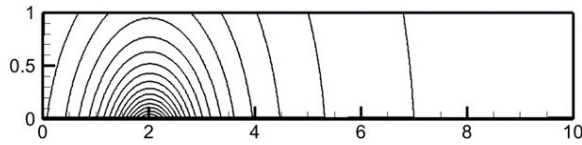
FIG. 6. Contour lines of magnetic field intensity.

in the channel at $(2.0, -0.5)$ in the channel, with no fluid flow. The magnetic intensity is calculated using the given equation [3]:

$$H(x, y) = \frac{|b|}{\sqrt{(x - a)^2 + (y - b)^2}},$$

where $a$ and $b$ are the locations of the magnetic sources.

Firstly, a stationary rigid filament (dimensionless length of 0.4) is positioned at $(2.0, 0.0)$, making an angle of $45°$ (clockwise direction) to the horizontal, as shown in Fig. 7. The location of the magnetic source is $(2.0, -0.5)$. The fluid is then allowed to flow along the channel, passing through the magnetic field and the stationary filament. The influence of the stationary filament and magnetic field on the fluid flow is studied by varying Mn at values of 0, 300, 500, and 1000, while keeping $Re = 10$, as demonstrated in Fig. 7.
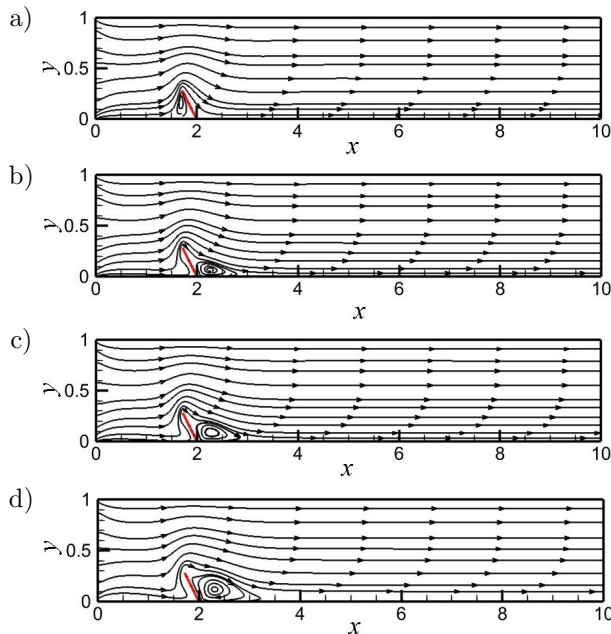


FIG. 7. Streamline plot for filament positioned at $\theta = 45°$ (clockwise direction) for fixed $Re = 10$, and a) Mn = 0, b) Mn = 300, c) Mn = 500, and d) Mn = 1000.

In Fig. 7, the formation and growth of the recirculation zone near the filament are observed with the increase in Mn values. Initially, when Mn = 0, the fluid flow interacts with the inclined filament, resulting in the formation of a recirculation zone upstream near the filament. As we increase Mn to 300, the recirculation zone forms downstream near the magnetic source, while the upstream recirculation zone diminishes. It is also noted that the flow vortex formation near the filament intensifies as the magnetic number increases from 300 to 1000. This indicates that a stronger magnetic field increases the size of the vortex near the immersed filament and the bottom wall.

Maintaining Mn at a constant value of 500, we varied the Reynolds numbers (10, 50, and 100), as illustrated in Fig. 8. It is observed that the vortex size increases as Re increases. Specifically, when Re = 100, a secondary vortex forms near the top wall, leading to the flow diversion on both sides of the wall.
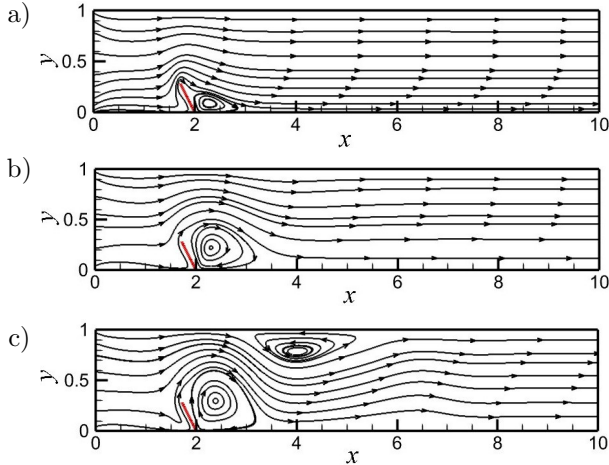


FIG. 8. Streamline plot for filament positioned at $\theta = 45°$ (clockwise direction) for fixed Mn = 500, and a) Re = 10, b) Re = 50, and c) Re = 100.

In Fig. 9, the velocity profile at the location of (2.3, 0.0) of the channel clearly shows the distortion of the velocity profile due to the interaction between the filament and the magnetic field. The negative velocities increase near the wall when both Mn and Re increase. This demonstrates that flow retardation occurs due to the combined influence of the magnetic field and the stationary filament near the magnetic source.

In the second set of simulations, we placed the rigid filament at an angle of 90°. Figure 10 illustrates the variation of streamlines of biomagnetic fluid flowing under the influence of the rigid vertical filament and magnetic field. The numerical simulations were carried out for Re = 10, with Mn values of 300, 500,
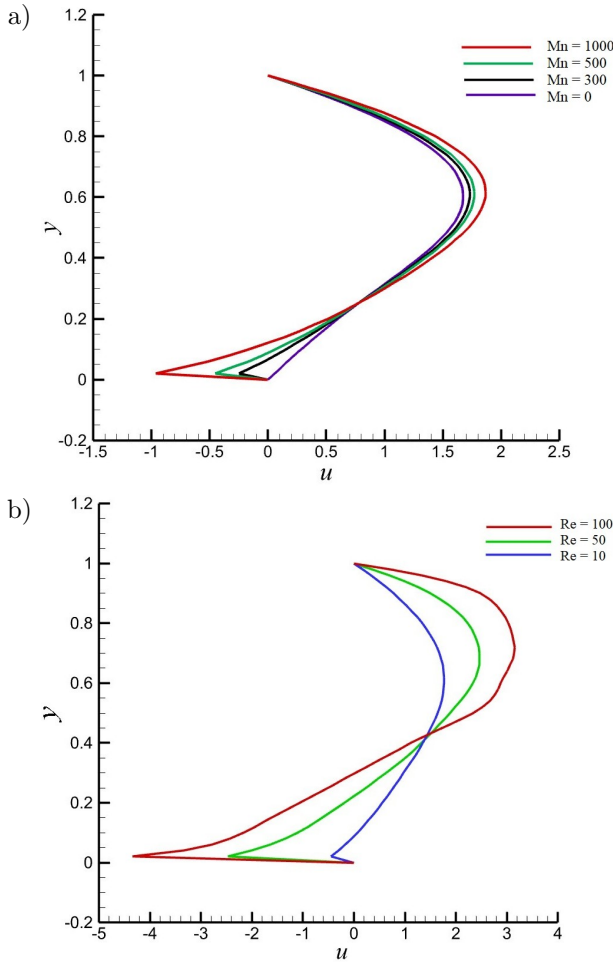
FIG. 9. Velocity profile at (2.3, 0.0): a) for fixed Re = 10, b) for fixed Mn = 500.

and 1000. It is observed that when Mn = 0, a flow vortex forms downstream of the vertical filament. As the magnetic number increases from 300 to 1000, there is a small increase in the size of the recirculation zone. However, this increase in size is considerably small due to the filament's vertical orientation and the magnetic field strength.

Next, we varied Re from 10 to 100 while keeping Mn fixed at 500. From Fig. 11, it is observed that there is an increase in the size of the flow vortex with an increase in Re. Also, a secondary vortex forms at the top of the wall. This shows that the influence of the magnetic field strength becomes more pronounced as the flow becomes less viscous (with an increase in Re). Figure 12a shows the velocity profile of the fluid at location (2.3, 0.0) for varying magnetic numbers (Mn = 0, 300, 500, and 1000). It can be observed that there is less deviation
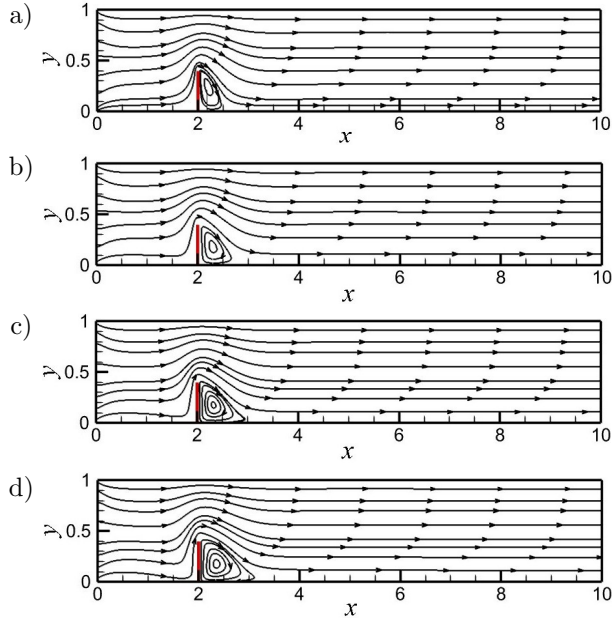
FIG. 10. Streamline plot for filament positioned at $\theta = 90°$ (clockwise direction) for fixed Re = 10, and a) Mn = 0, b) Mn = 300, c) Mn = 500, and d) Mn = 1000.



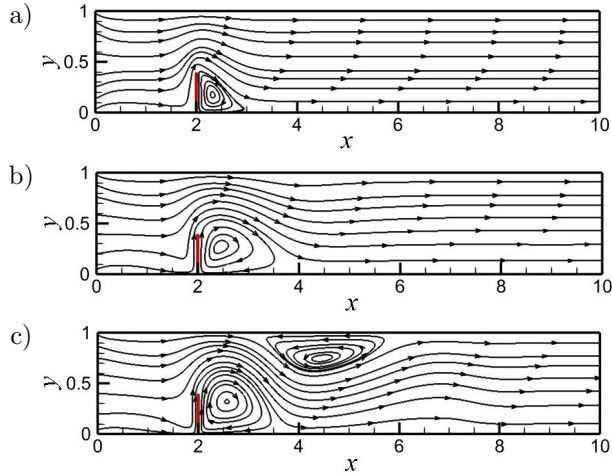FIG. 11. Streamline plot for filament positioned at $\theta = 90°$ (clockwise direction) for fixed Mn = 500, and a) Re = 10, b) Re = 50, and c) Re = 100.

in the velocity profile with an increase in the magnetic number compared to when Mn is 0. The deviation is only observed near the wall close to the location of the magnetic source, where negative velocities appear. This shows that the effect of the magnetic force is localized near the location of the magnetic source.
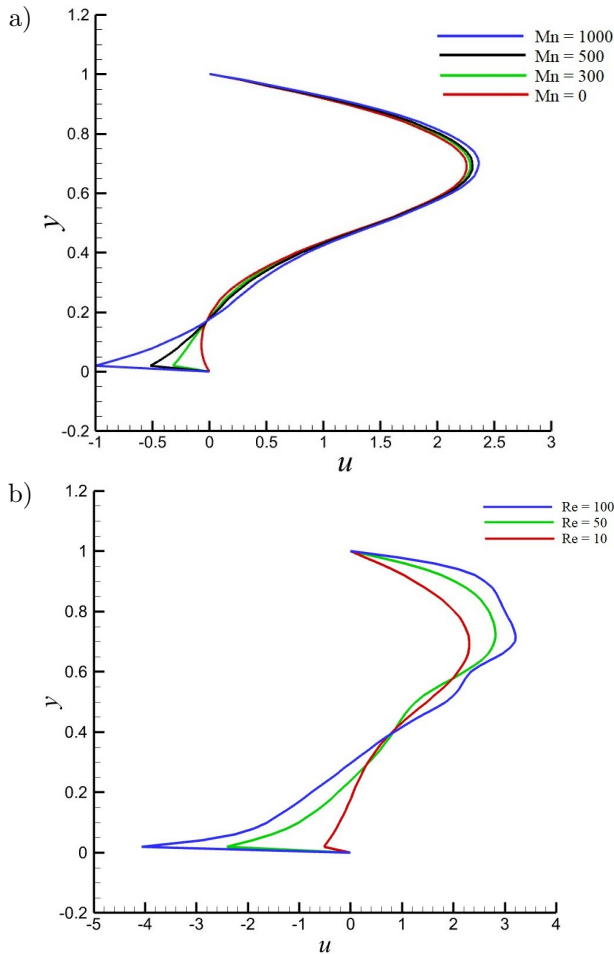
FIG. 12. Velocity profile at $(2.3, 0.0)$: a) for fixed $Re = 10$, b) for fixed $Mn = 500$.

Simultaneously, a greater deviation in the velocity profile is observed in Fig. 12b as Re increases.

Finally, simulations for the case of a filament positioned at an angle of $135°$ are carried out using the numerical model. Similar to the previous cases, a parametric study is conducted by fixing $Re = 10$ and varying Mn from 0 to 1000, as shown in Fig. 13. When $Mn = 0$, recirculation forms near the inclined filament downstream, similar to the case of the vertical filament placed at angle of $90°$. A similar trend of an increase in the size of the vortex is observed as Mn increases from 300 to 1000. However, when Mn is 300 or 500, there is negligible change in the size of the vortex.

Similarly, by keeping Mn constant and varying Re from 10 to 100 (shown in Fig. 14), we observed that the vortex size increases from $Re = 10$ to 50, but there
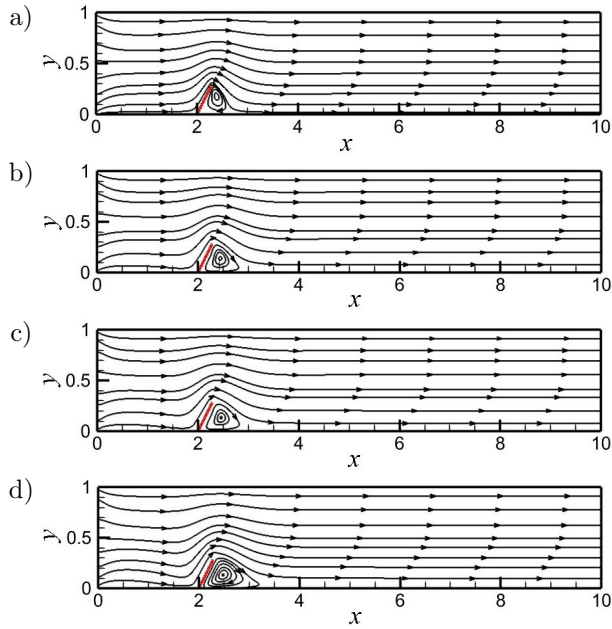
FIG. 13. Streamline plot for filament positioned at $\theta = 135°$ (clockwise direction) for fixed Re = 10, and a) Mn = 0, b) Mn = 300, c) Mn = 500, and d) Mn = 1000.



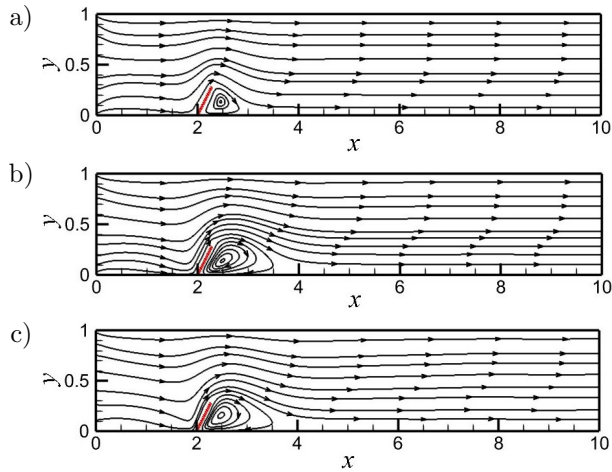FIG. 14. Streamline plot for filament positioned at $\theta = 135°$ (clockwise direction) for fixed Mn = 500, and a) Re = 10, b) Re = 50, and c) Re = 100.

is less increase in the size of the vortex from Re = 50 to 100. This could be due to the combined effect of more influence of the magnetic field strength (caused by the increase in Re) and that of filament orientation. Unlike the previous cases of filament orientation, no secondary vortex appears near the top wall. The velocity

profiles shown in Fig. 15 reveal that the deviation of the profile near the magnetic source is almost identical for Mn = 300 and 500. This shows that the orientation of the filament causes less influence on the magnetic intensity strength of the fluid away from the magnetic source.
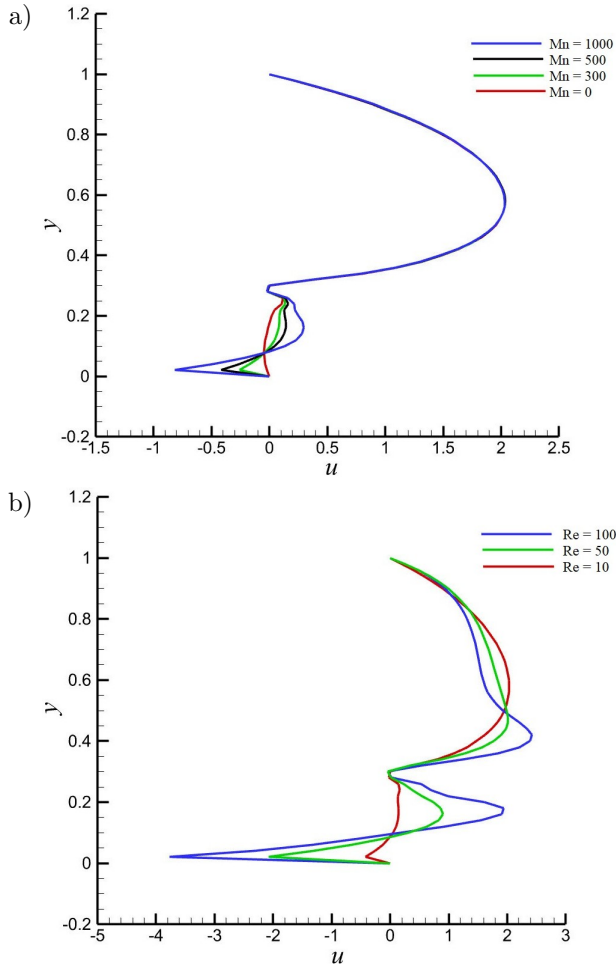


FIG. 15. Velocity profile at (2.3, 0.0): a) for fixed Re = 10, b) for fixed Mn = 500.

## 4. Conclusion

The current study investigated the flow of biomagnetic fluid in a channel employing a 2D IBM-based computational model and uncovered the complex relationships between magnetic forces, Re, and filament orientation. The introduction of a magnetic field in the channel flow generated a vortex, and the size of the vortex increased with an increase in Re and Mn. It is observed that the ori-

entation of the filament at $\theta = 45°$ and $90°$ significantly affects the formation of multiple recirculations, whereas there is no formation of secondary vortices at $\theta = 135°$. The velocity profile reveals that the flow is slowed down near the magnetic source, with higher negative velocities observed when the filament orientation is $\theta = 90°$ and the Re is 100. These findings illustrate the intricate relationship between flow dynamics, the magnetic field, and the orientation of immersed structures.

## References

1. Y. Haik, V. Pai, C. Chen, Development of bio-magnetic fluid dynamics, [in:] *Proceedings of the IX International Symposium on Transport Properties in Thermal Fluid Engineering*, Singapore, Pacific Center of Thermal Fluid Engineering, S.H. Winoto, Y.T. Chew, N.E. Wijeysundera [Eds.], Hawaii, USA, pp. 121–126, 1996.

2. L. Pauling, C. Coryell, The magnetic properties and structure of hemoglobin, oxyhemoglobin and carbonmonoxy haemoglobin, [in:] *Proceedings of the National Academy of Science*, 21, 1936.

3. V.C. Loukopoulos, E.E. Tzirtzilakis, Biomagnetic channel flow in spatially varying magnetic field, *International Journal of Engineering Science*, **42**(5–6): 571–590, 2004.

4. E.E. Tzirtzilakis, Biomagnetic fluid flow channel with stenosis, *Physic D Nonlinear Phenomena*, **237**: 66–81, 2008.

5. M.R. Habibi, M. Ghassemi, A. Shahidian, Investigation of biomagnetic fluid flow under nonuniform magnetic fields, *Nanoscale Microscale Thermophysical Engineering*, **16**(1): 64–77, 2012.

6. S. Kenjeres, Numerical analysis of blood flow in realistic arteries subjected to strong nonuniform magnetic fields, *International Journal of Heat and Fluid Flow*, **29**(3): 752–764, 2008.

7. S.M. Mousavi, M. Farhadi, K. Sedighi, Effect of non-uniform magnetic field on biomagnetic fluid flow in a 3D channel, *Applied Mathematical Modelling*, **40**(15–16): 7336–7348, 2016.

8. D.K. Ravada, R. Maniyeri, Numerical simulation of two-dimensional biomagnetic shear flow, *Materials Today Proceedings*, 2023, https://doi.org/10.1016/j.matpr.2023.01.127.

9. C.S. Peskin, Numerical analysis of blood flow in the heart, *Journal of Computational Physics*, **25**(3): 220–252, 1977.

10. M.C. Lai, C.S. Peskin, An immersed boundary method with formal second-order accuracy and reduced numerical viscosity, *Journal of Computational Physics*, **160**(2): 705–719, 2000.

11. R. Maniyeri, S. Kang, Numerical study on the rotation of an elastic rod in a viscous fluid using an immersed boundary method, *Journal of Mechanical Science and Technology*, **26**(5): 1515–1522, 2012.

12. R. Maniyeri, S. Kang, Numerical study on bacterial flagellar bundling and tumbling in a viscous fluid using an immersed boundary method, *Applied Mathematical Modelling*, **38**(14): 3567–3590, 2014.

13. M. Kanchan, R. Maniyeri, Numerical analysis of the buckling and recuperation dynamics of flexible filament using an immersed boundary framework, *International Journal of Heat and Fluid Flow*, **77**: 256–277, 2019.

14. J. Basil Eldoe, M. Kanchan, R. Maniyeri, Modeling rigid filament interaction under oscillatory flow using immersed boundary method, *Materials Today Proceedings*, **56**(2): 785–790, 2022, https://doi.org/10.1016/j.matpr.2022.02.257.

15. M. Kanchan, R. Maniyeri, Numerical simulation of buckling and asymmetric behavior of flexible filament using temporal second-order immersed boundary method, *International Journal of Numerical Methods for Heat & Fluid Flow*, **30**(3): 1047–1095, 2020.

16. D.S. Kershaw, The incomplete Cholesky conjugate gradient method for the iterative solution of systems of linear equations, *Journal of Computational Physics*, **26**(1): 43–65, 1978.

17. Z. Guo, B. Shi, N. Wang, Lattice BGK model for incompressible Navier–Stokes equation, *Journal of Computational Physics*, **165**(1): 288–306, 2000.

18. M. Coutanceau, R. Bouard, Experimental determination of the main features of the viscous flow in the wake of a circular cylinder in uniform translation. Part 2. Unsteady flow, *Journal of Fluid Mechanics*, **79**(2): 257–272, 1977.

19. L. Zhu, C.S. Peskin, Simulation of a flapping flexible filament in a flowing soap film by the immersed boundary method, *Journal of Computational Physics*, **179**(2): 452–468, 2002.

20. W.X. Huang, S.J. Shin, H.J. Sung, Simulation of flexible filaments in a uniform flow by the immersed boundary method, *Journal of Computational Physics*, **226**(6): 2206–2228, 2007.